

## Domain rearrangement in ferroelectric Bi<sub>4</sub>Ti<sub>3</sub>O<sub>12</sub> thin films studied by in situ optical second harmonic generation

Yaniv Barad, James Lettieri, Chris D. Theis, Darrell G. Schlom, and Venkatraman Gopalan

Citation: *Journal of Applied Physics* **90**, 3497 (2001); doi: 10.1063/1.1402673

View online: <http://dx.doi.org/10.1063/1.1402673>

View Table of Contents: <http://scitation.aip.org/content/aip/journal/jap/90/7?ver=pdfcov>

Published by the **AIP Publishing**

### Articles you may be interested in

[Study of defect-dipoles in an epitaxial ferroelectric thin film](#)

*Appl. Phys. Lett.* **96**, 052903 (2010); 10.1063/1.3298362

[90° a – b domains in epitaxial ferroelectric Bi<sub>3.25</sub>La<sub>0.75</sub>Ti<sub>3</sub>O<sub>12</sub> films](#)

*Appl. Phys. Lett.* **85**, 2029 (2004); 10.1063/1.1788879

[Erratum: “Probing domain microstructure in ferroelectric Bi<sub>4</sub>Ti<sub>3</sub>O<sub>12</sub> thin films by optical second harmonic generation” \[\*J. Appl. Phys.\* \*\*89\*\*, 1387 \(2001\)\]](#)

*J. Appl. Phys.* **89**, 5230 (2001); 10.1063/1.1360714

[Probing domain microstructure in ferroelectric Bi<sub>4</sub>Ti<sub>3</sub>O<sub>12</sub> thin films by optical second harmonic generation](#)

*J. Appl. Phys.* **89**, 1387 (2001); 10.1063/1.1334641

[Electric field induced domain rearrangement in potassium niobate thin films studied by in situ second harmonic generation measurements](#)

*J. Appl. Phys.* **81**, 865 (1997); 10.1063/1.364222

The new SR865 **2 MHz Lock-In Amplifier ... \$7950**





Chart recording



FFT displays



Trend analysis

**Features**

- Intuitive front-panel operation
- Touchscreen data display
- Save data & screen shots to USB flash drive
- Embedded web server and iOS app
- Synch multiple SR865s via 10 MHz timebase I/O
- View results on a TV or monitor (HDMI output)

**Specs**

- 1 mHz to 2 MHz
- 2.5 nV/√Hz input noise
- 1 μs to 30 ks time constants
- 1.25 MHz data streaming rate
- Sine out with DC offset
- GPIB, RS-232, Ethernet & USB

**SRS Stanford Research Systems**  
www.thinkSRS.com · Tel: (408)744-9040

# Domain rearrangement in ferroelectric $\text{Bi}_4\text{Ti}_3\text{O}_{12}$ thin films studied by *in situ* optical second harmonic generation

Yaniv Barad, James Lettieri, Chris D. Theis, Darrell G. Schlom, and Venkatraman Gopalan<sup>a)</sup>

*Department of Materials Science and Engineering and Material Research Institute, Pennsylvania State University, University Park, Pennsylvania 16801*

(Received 4 June 2001; accepted for publication 19 July 2001)

Electric-field induced rearrangement of domain microstructure in an epitaxial thin film of  $\text{Bi}_4\text{Ti}_3\text{O}_{12}$  on a  $\text{SrTiO}_3$  (001) substrate is studied by optical second harmonic generation measurements. The input polarization dependence of the second harmonic signal exhibits spatial symmetries that reflect the presence of eight different domain variants present in the film. Changes in these symmetries with the application of electric field are experimentally studied at 23 °C and 60 °C, and theoretically modeled to extract the hysteresis loops that reflect quantitative changes in the fraction of domain variants. A strong correlation is observed between the dc electrical conductance (as distinct from transient currents) and the ferroelectric domain state of the film, which is proposed to arise from the creation and destruction of charged domain walls within the film with applied field. © 2001 American Institute of Physics. [DOI: 10.1063/1.1402673]

## I. INTRODUCTION

Ferroelectric bismuth titanate,  $\text{Bi}_4\text{Ti}_3\text{O}_{12}$ , which belongs to the Aurivillius phases, is of interest in nonvolatile memory due to excellent fatigue resistance during repeated polarization reversals with electric field.<sup>1,2</sup> The spontaneous polarization in a monoclinic unit of  $\text{Bi}_4\text{Ti}_3\text{O}_{12}$  has components along both the  $a$  and  $c$  crystallographic directions, where  $a$ - $c$  forms the glide plane (010). Both  $a$  and  $c$  components of the polarization can be independently reversed, thus resulting in four different classes of domain walls and 18 wall configurations.<sup>3</sup> All these configurations are not readily distinguishable in a thin film by conventional x-ray diffraction or transmission electron microscopy. In a recent article, we showed how probing the second harmonic generation (SHG) response of a  $\text{Bi}_4\text{Ti}_3\text{O}_{12}$  film with a complex domain microstructure can provide many of these domain distinctions in a quantitative manner.<sup>4</sup>

In this work, we use our previously reported experimental technique and theoretical framework of SHG probing of  $\text{Bi}_4\text{Ti}_3\text{O}_{12}$  films,<sup>4</sup> to study the domain rearrangement process under an external electric field in these films. These studies allow a direct, quantitative probing of the variation of different domain fractions as a function of applied electric field. Correlation of the variation in domain statistics with the electrical currents through the film shows that the domain state strongly influences the dc conductance in the material.

## II. FILM EPITAXY AND DOMAIN MICROSTRUCTURE

The  $\text{Bi}_4\text{Ti}_3\text{O}_{12}$  thin film studied here was grown on a  $\text{SrTiO}_3$  (001) substrate using molecular beam epitaxy as previously reported in detail.<sup>4,5</sup> The lattice parameters of the cubic  $\text{SrTiO}_3$  (001) substrate,  $a' = 3.9050$  Å closely match

along its diagonal of  $a''\sqrt{2}$ , with the lattice parameters  $a = 5.4500$  Å and  $b = 5.4059$  Å of the monoclinic  $\text{Bi}_4\text{Ti}_3\text{O}_{12}$ . (The other lattice parameters are  $c = 32.832$  Å, and  $\beta = 90.00^\circ$ ).<sup>6</sup> The lattice planes  $b$ - $c$ ,  $c$ - $a$ , and  $a$ - $b$  of  $\text{Bi}_4\text{Ti}_3\text{O}_{12}$  are, respectively, denoted as (100), (010), and the (001) planes. As reported before, the epitaxial orientational relationship is  $\text{SrTiO}_3(001)[110]//\text{Bi}_4\text{Ti}_3\text{O}_{12}(001)[100]$ . In this configuration, there are eight possible domain configurations of  $\text{Bi}_4\text{Ti}_3\text{O}_{12}$  as shown schematically in Fig. 1. Each of the possible domains has a monoclinic unit cell, which deviates only slightly from the orthorhombic unit cell. The polarization axis forms an angle of  $\sim 4.5^\circ$  from the crystallographic  $a$  axis in the  $a$ - $c$  (010) plane.

Figure 2 shows the various domain walls that can arise from a combination of these domain variants. In particular, referring to the pseudo-orthorhombic planes of  $\text{Bi}_4\text{Ti}_3\text{O}_{12}$ , four main types of domain walls can exist: (I) Nearly  $90^\circ$  domain walls along the (110) planes. (II) Domain walls separating variants with opposite  $a$  component of polarization. These walls are either neutral (001) planes or charged (100) planes. (III) Domain walls separating variants with opposite  $c$  component of polarization. These walls are either neutral (100) planes or charged (001) planes. (IV)  $180^\circ$  domain walls parallel to the (010) planes and separating domains with opposite sense of both  $a$  and  $c$  components of polarization. Transmission electron microscopy reveals a network of near  $90^\circ$  domain walls with the average lateral size of such domains  $\sim 100$ – $200$  nm.<sup>4</sup>

Based on the above discussion, we define four classes of domain variants  $X+$ ,  $X-$ ,  $Y+$ , and  $Y-$  according to whether the  $a$  component of polarization points in the  $\text{SrTiO}_3$   $[110]$ ,  $[\bar{1}10]$ ,  $[1\bar{1}0]$ , or  $[\bar{1}\bar{1}0]$  directions, or alternatively  $(+x, -x, +y, -y)$  directions in Fig. 1, respectively. In the following sections, we describe how changes in the domain statistics of  $X+$ ,  $X-$ ,  $Y+$ , and  $Y-$  domains can be distinguished by SHG measurements.

<sup>a)</sup>Author to whom correspondence should be addressed; electronic mail: vgp@psu.edu

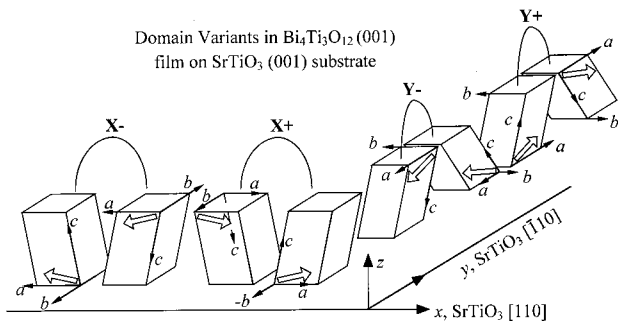


FIG. 1. A schematic description of the eight possible domain configurations of the  $\text{Bi}_4\text{Ti}_3\text{O}_{12}$  thin film on a  $\text{SrTiO}_3(001)$  substrate. Each of the possible domains has a monoclinic unit cell, with lattice parameters  $a = 5.4500 \text{ \AA}$  and  $b = 5.4059 \text{ \AA}$ ,  $c = 32.832 \text{ \AA}$ , and  $\beta = 90.00^\circ$ , which slightly deviates from the orthorhombic unit cell. The polarization axis forms an angle of  $\approx 4.5^\circ$  from the crystallographic  $a$  axis in the  $a$ - $c$  plane as shown by wide arrows. Both the tilt angle  $\beta$  and the angle of polarization from the  $a$  axis are shown exaggerated in the schematic.

### III. *In situ* SECOND HARMONIC GENERATION OF ELECTRIC FIELD POLING OF $\text{Bi}_4\text{Ti}_3\text{O}_{12}$ FILMS

#### A. Experimental Procedure

A schematic description of the experimental setup is shown in Fig. 3. The fundamental beam from a 10 Hz  $Q$ -switched Nd:YAG laser ( $\lambda = 1064 \text{ nm}$ ) is passed through a series of beam splitters to cut its intensity to approximately 10 mW. The beam is then propagated through a polarizer, a half wave plate, focusing lens ( $f = 500 \text{ mm}$ ) and a long-wave pass filter to absorb any residual second harmonic light. The half wave plate is situated on a computer controlled rotating stepper motor to allow the continuous change of the polarization at the input. The sample is placed 50 mm in front of the focal point of the focusing lens, where the beam diameter is approximately 1.2 mm, and the energy density is below the damage threshold. The sample is situated on a small heating stage inside a water-cooled chamber and it is held with the thin film at the exit side of the fundamental beam. The hot stage was capable of reaching temperatures as high as  $700^\circ\text{C}$ , with long-term stability better than  $1^\circ\text{C}$  over 10 h.

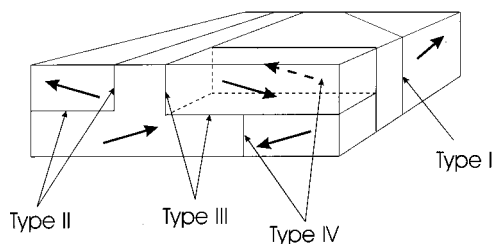


FIG. 2. A schematic illustration of four different types of domain walls possible in the  $\text{Bi}_4\text{Ti}_3\text{O}_{12}$  thin film. (I) Nearly  $90^\circ$  domain walls along the (110) plane. (II) Domain walls separating variants with opposite  $a$  component of polarization. These walls are either neutral (001) ( $a$ - $b$ ) planes or charged (100) ( $b$ - $c$ ) planes. (III) Domain walls separating variants with opposite  $c$  component of polarization. These walls are either neutral (100) ( $b$ - $c$ ) planes or charged (001) ( $a$ - $b$ ) planes. (IV)  $180^\circ$  domain walls parallel to the (010) ( $a$ - $c$ ) planes and separating domains with opposite sense of both  $a$  and  $c$  components of polarization. The arrows denote the direction of polarization within each domain.

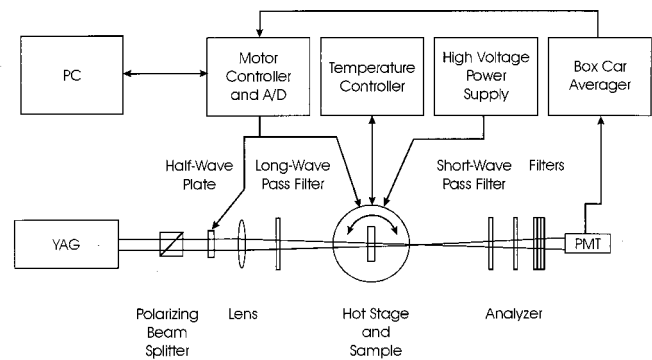


FIG. 3. A schematic description of the experimental setup. The fundamental beam from a YAG source is incident normally on the sample. A half-wave plate controls the polarization of the fundamental light, at  $1064 \text{ nm}$ , at the input. A focusing lens is used to reduce the beam size on the sample to  $\sim 1.2 \text{ mm}$  in diameter. The SHG light is filtered from the main beam and its polarization is analyzed using a polarizer. The PMT detects the SHG intensity at the measured polarization. The sample is situated inside a temperature controlled stage with electrodes attached to it to allow for a bias voltage across the sample. A boxcar integrator is used for measuring the PMT signal, and the averaged signal is read by a computer via an A/D card.

An external electric field is applied on the sample using two high temperature resistant springlike electrodes, attached to the hot stage, which also hold the sample in its place. The sample arrangement is shown schematically in Fig. 4. Four gold electrodes are sputtered on the sample with a gap of  $\sim 3 \text{ mm}$  between pairs of adjacent electrodes to assure enough clearance for the beam. The beam is pointed to the center of the gap between two of the electrodes and the spring-loaded electrodes are attached to the plated electrodes. The output beam is passed through a short-wave pass filter to absorb the fundamental light at  $1064 \text{ nm}$  and the second harmonic signal at  $532 \text{ nm}$  is analyzed with a polarizer aligned either along the  $x$  axis ( $\text{SrTiO}_3 [110]$ ) or  $y$  axis ( $\text{SrTiO}_3 [\bar{1}\bar{1}0]$ ). The beam is then propagated to the photomultiplier tube (PMT) and its intensity is lowered using neutral density filters if needed. The signal from the PMT is fed to a gated integrator

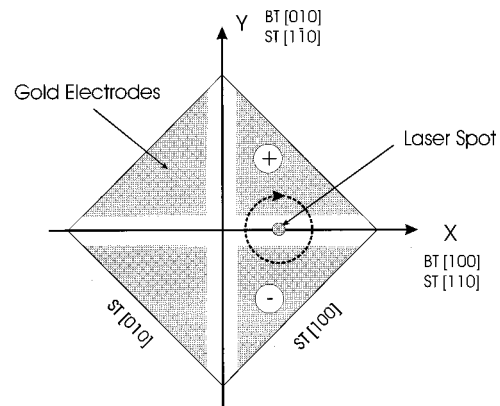


FIG. 4. A schematic configuration of the thin film sample. The sample is divided into four measurable areas by sputtering the four gold electrodes on top of the film. The light is incident at the center of the gap between two of the electrodes with its polarization changing by  $360^\circ$  for each measurement, as described by the dashed arrow. A bias voltage is applied across the film with the field direction along the  $\pm y$  axis defined in Fig. 1.

and a boxcar averager. The averaged output is read to the computer via an analog to digital (A/D) converter.

Once the sample is heated and stabilized at the desired temperature, a measurement with no voltage across the sample is taken. The measurement starts with the light polarization parallel to the  $\text{Bi}_4\text{Ti}_3\text{O}_{12}$  thin film [010] and with the analyzer either parallel or perpendicular to that direction. (The  $\text{SrTiO}_3$  substrate is cubic, and it was confirmed that it does not result in any second harmonic response.) The incident polarization is changed by rotating the half-wave plate, while keeping the analyzer fixed. The measurement is made once with the analyzer along the  $x$  axis and once along the  $y$  axis labeled in Fig. 1. These measurements provide information on the specific distribution of domains in the area probed. In general, a different area on the film gives slightly different polar plots. However, all these plots can be analyzed within the same theoretical framework given in our previous work.<sup>4</sup> The same procedure is now repeated with a voltage applied across the sample.

### B. Theoretical model

In the following we give a brief description of the theoretical model. For a detailed description, see Ref. 4. In order to describe the expected SHG intensity from the thin film  $I^{2\omega}$ , the net polarization at the second harmonic frequency  $P^{2\omega}$  should be calculated along a global coordinate system  $(x, y, z)$  of the substrate (shown in the schematic of Fig. 2).

We assume the fundamental wave is a plane wave propagating along the  $z$  direction and incident normal to the film. This assumption has been found to be quite good,<sup>7</sup> due to the fact that the incident Gaussian beam is very weakly focused (beam divergence  $\sim 0.01$  rad), and the sample is placed close to the focal point where the beam incident on the sample is large (1.2 mm diameter). The film thickness studied here is  $t \sim 0.1 \mu\text{m}$ . This is smaller than the coherence length  $l_c = \lambda/2(n^{2\omega} - n^\omega)$  for phase matched SHG in the film, which for  $a$ -axis polarized fundamental light at 1064 nm, is  $l_c \sim 3.36 \mu\text{m}$ , while for  $b$ -polarized light,  $l_c \sim 2.89 \mu\text{m}$ . Bulk index dispersion relations of  $\text{Bi}_4\text{Ti}_3\text{O}_{12}$  crystals were used to estimate the coherence lengths.<sup>8</sup> The incident electric field  $E^\omega$  has a polarization rotating in the  $x$ - $y$  plane, forming an angle  $\theta$  with the  $y$  axis. The incident electric fields along  $x$  and  $y$  axes are  $E_x^\omega = E^\omega \sin \theta$  and  $E_y^\omega = E^\omega \cos \theta$ . During the measurement the output analyzer is fixed either along the  $x$  or  $y$  axis. For normal incidence, as in our case,  $E_z = 0$  and therefore contributions to the SHG field are only due to  $d_{11}$ ,  $d_{12}$ , and  $d_{26}$ . Following the theoretical derivation outlined in Ref. 7, the nonlinear polarizations created in the four classes of domain variants can be calculated as a function of  $E^\omega$  and  $\theta$  as shown in Table I. Note that the nonlinear polarizations of the domain variants  $X+$  and  $X-$  are identical in magnitude, but differ by a minus sign indicating a phase difference of  $\pi$  or  $180^\circ$ . The same is true for nonlinear polarizations of domain variants  $Y+$  and  $Y-$ . The relative phase shift of  $\pi$  between two domain variants results in a net destructive interference of the second harmonic fields since the film thickness is much smaller than coherence length. These nonlinear polarizations  $P^{2\omega}$  now radiate light at a fre-

TABLE I. Nonlinear polarization for the four variants shown schematically in Fig. 1.

Variant	$P_x$ (analyzer $\parallel x$ )	$P_y$ (analyzer $\parallel y$ )
$X+$	$\frac{1}{\sqrt{2}}(d_{11} \sin^2 \theta + d_{12} \cos^2 \theta)(E^\omega)^2$	$\frac{1}{\sqrt{2}}d_{26} \sin 2\theta(E^\omega)^2$
$X-$	$-P_x^{X+}$	$-P_y^{Y+}$
$Y+$	$\frac{1}{\sqrt{2}}d_{26} \sin 2\theta(E^\omega)^2$	$\frac{1}{\sqrt{2}}(d_{11} \cos^2 \theta + d_{12} \sin^2 \theta)(E^\omega)^2$
$Y-$	$-P_x^{Y+}$	$-P_y^{X+}$

quency of  $2\omega$ , with intensity  $I^{2\omega} \propto P^{2\omega} \cdot (P^{2\omega})^*$ , where the  $*$  superscript represents the complex conjugate of the nonlinear polarization. This intensity is given by

$$I_j^{2\omega} = K_{1,j}(\sin^2 \theta + K_{2,j} \cos^2 \theta)^2 + K_{3,j} \sin^2 2\theta + K_{4,j}(\sin^2 \theta + K_{2,j} \cos^2 \theta) \sin 2\theta, \quad (1)$$

where  $j = x$  or  $y$  denotes the polarization direction, and  $K_{i,j}$  are the phenomenological fitting parameters. Using Table I, we can show the following relations between these parameters and the physical quantities:

$$\frac{d_{12}}{d_{11}} = K_{2,x} = (K_{2,y})^{-1}, \quad (2)$$

$$\left(\frac{d_{26}}{d_{12}}\right)^4 = \left(\frac{K_{3,x}}{K_{1,x}(K_{2,x})^2}\right) \left(\frac{K_{3,y}}{K_{1,y}}\right), \quad (3)$$

$$\left(\frac{d_{26}}{d_{11}}\right)^4 = \left(\frac{K_{3,y}}{K_{1,y}(K_{2,y})^2}\right) \left(\frac{K_{3,x}}{K_{1,x}}\right), \quad (4)$$

$$\cos^2 \Gamma = \frac{(K_{4,x})^2}{4K_{1,x}K_{3,x}} = \frac{(K_{4,y})^2}{4K_{1,y}K_{3,y}}, \quad (5)$$

and

$$\left(\frac{\Delta A_x}{\Delta A_y}\right)^4 = \left(\frac{K_{3,y}}{K_{1,y}(K_{2,y})^2}\right) \left(\frac{K_{1,x}}{K_{3,x}}\right), \quad (6)$$

Here,  $d_{ij}$  are the nonlinear coefficients of  $\text{Bi}_4\text{Ti}_3\text{O}_{12}$ , and  $\Gamma$  is a phase shift defined as  $\Gamma = 2\omega/c(n_b^{2\omega} - n_a^{2\omega}) \cdot t$ , where  $n_b$  and  $n_a$  are the refractive indices of  $\text{Bi}_4\text{Ti}_3\text{O}_{12}$  at the SHG frequency, along the crystallographic  $b$  and  $a$  axes, respectively, and  $t$  is the film thickness. The net thickness fractions  $\Delta A_x$  and  $\Delta A_y$  represent local microstructural information as defined below. Let  $A^X$  represent the total area fraction of the probed film area composed of  $X+$  and  $X-$  domains. Consider light passing through the film thickness in an area  $dA^X$ . Referring to the domain microstructure in  $\text{Bi}_4\text{Ti}_3\text{O}_{12}$  (see Fig. 2), the  $X+$  and an  $X-$  domain variants are separated by type II domain walls which are either neutral (001) planes or charged (100) planes, where the plane indices refer to the pseudo-orthorhombic unit cell of  $\text{Bi}_4\text{Ti}_3\text{O}_{12}$ . The  $a$ - $b$  domain walls will run parallel to the growth surface ( $\text{SrTiO}_3$  (001)), and therefore give rise to domain patterns in the cross-sectional thickness of the film as well. The light therefore passes through a thickness fraction  $t^{X+}$  of the  $X+$  domain and  $t^{X-}$  of the  $X-$  domain, making the net nonlinear

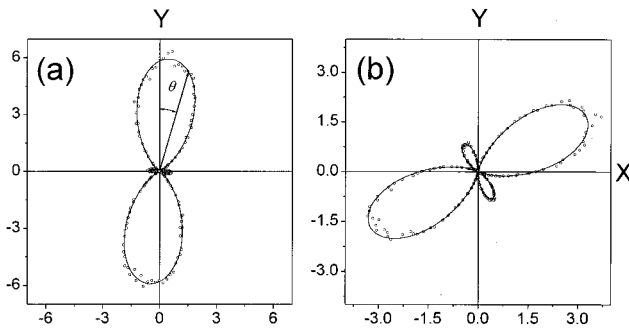


FIG. 5. Polar plots of the SHG intensity  $I^{2\omega}$  ( $\lambda=532$  nm) as a function of input polarization angle  $\theta$  ( $\lambda=1064$  nm) for the output polarization of the SHG light along (a)  $\text{Bi}_4\text{Ti}_3\text{O}_{12}$  [010] ( $y$  axis) and (b)  $\text{Bi}_4\text{Ti}_3\text{O}_{12}$  [100] ( $x$  axis). The data shown here were measured at room temperature on an as-deposited  $\text{Bi}_4\text{Ti}_3\text{O}_{12}$  film on the  $\text{SrTiO}_3(100)$  substrate with no bias voltage applied across the film. The experimental data are shown in circles, while the solid line is a nonlinear fit obtained based on Eq. (1) derived from the theoretical model presented in this article. The arrow in (a) represents the magnitude of the SHG light and  $\theta$  indicates the direction of polarization of the fundamental light with respect to the  $y$  axis.

polarization generated by the combination of the two domain variants proportional to  $(t^{X+} - t^{X-})(P^{X+})^{2\omega}$ . Then the net thickness fractions  $\Delta A_x$  is defined as  $\Delta A_x = \int_0^{A_x} (t^{X+} - t^{X-}) dA^X$ . Similarly, considering the  $Y+$  and  $Y-$  domains in an area  $dA^Y$  of the growth plane, the net thickness fraction  $\Delta A_y$  is defined as  $\Delta A_y = \int_0^{A_y} (t^{Y+} - t^{Y-}) dA^Y$ . These relationships reflect the net destructive interference of the second harmonic electric fields created by  $X+(Y+)$  and  $X-(Y-)$  domains due to the  $\pi$  phase shift between the two fields. This analysis therefore assumes *complete phase correlation*, which implies that the second harmonic response of all domain variants is phase correlated. This assumption is justified in our present case since the domain sizes of  $X+$  and  $X-$  variants are on the order of 100–200 nm in the film growth plane, which is less than the wavelength of light.<sup>4</sup>

The fitting coefficients  $K_{i,j}$  can be determined from the experimental measurements. Equations (2) and (3) can be used to determine two independent ratios;  $d_{12}/d_{11}$  and  $d_{26}/d_{11}$ . Equation (4) then provides a consistency check for the ratio  $d_{26}/d_{12}$ . The phase shift  $\Gamma$  can be determined from Eq. (5), which in turn can be used to determine the material birefringence  $\Delta n = (n_b^{2\omega} - n_a^{2\omega})$ . Note that the parameters  $d_{12}/d_{11}$ ,  $d_{26}/d_{11}$ , and  $\Delta n$  are *intrinsic* material properties, and can be determined *independent* of the domain microstructure, i.e., the relative fractions of the eight different types of domain variants. Equation (6) provides new *microstructural* information,  $\Delta A_x/\Delta A_y$ , in the area probed.

## IV. RESULTS AND DISCUSSION

### A. Changes in domain statistics with electric field

The intensity of the second harmonic signal generated in the film was measured as a function of the input polarization, and analyzed along the two optical axes of the sample. The measurements procedure is identical to the procedure reported in Ref. 4, with the addition of the applied electric field across the film and changing the film temperature. Figure 5 shows the polar plot of the SHG signal measured at room

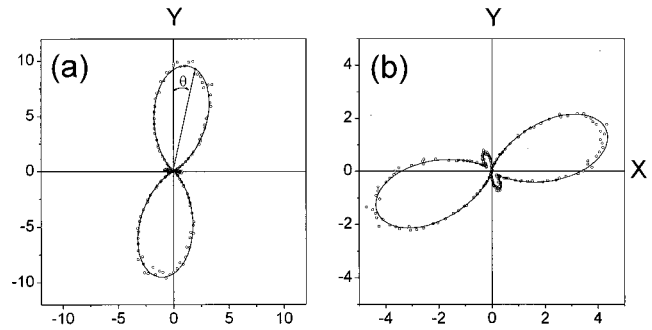


FIG. 6. Polar plots of the SHG intensity  $I^{2\omega}$  ( $\lambda=532$  nm) as a function of input polarization angle  $\theta$  ( $\lambda=1064$  nm) for the output polarization of the SHG light along (a)  $\text{Bi}_4\text{Ti}_3\text{O}_{12}$  [010] ( $y$  axis), and (b)  $\text{Bi}_4\text{Ti}_3\text{O}_{12}$  [100] ( $x$  axis). The data shown here were measured at room temperature on an as-deposited  $\text{Bi}_4\text{Ti}_3\text{O}_{12}$  film on the  $\text{SrTiO}_3(100)$  substrate with a bias voltage of  $-2$  kV applied across surface electrodes (3 mm apart, see Fig. 4) with the field in the  $-y$  direction (see Fig. 1) The experimental data is shown in circles, while the solid line is a nonlinear fit obtained based on Eq. (1) derived from the theoretical model presented in this article. The arrow in (a) represents the magnitude of the SHG light and  $\theta$  indicates the direction of polarization of the fundamental light with respect to the  $y$  axis.

temperature with no voltage applied across the sample. This was the state of the first measurement on an as-deposited film with no prior electric field poling history. The dots represent the experimental data points and the solid line is the nonlinear fit to the experimental data based on Eq. (1). From the fitting parameters, the material and microstructural parameters were found to be  $d_{11}/d_{12} = -3.54 \pm 0.3$ ,  $|d_{26}/d_{11}| = 0.41 \pm 0.08$ ,  $>\Delta n = 0.079 \pm 0.015$ , and  $\Delta A_y/\Delta A_x = 2.25 \pm 0.06$ . The arrow shows the magnitude of the SHG light and  $\theta$  is the angle measured from the  $y$  axis. On application of an electric field  $E_y$  at room temperature along the  $\pm y$  directions, the shape of these polar plots changes. This electric field is expected to directly change the relative domain statistics of  $Y+$  and  $Y-$  domains, and therefore the quantity  $\Delta A_y$ . In addition, changes in the  $X+$  and  $X-$  domains are also possible through the movement of nearly  $90^\circ$  domain walls of type I shown in Fig. 2. The changes in polar plots is seen by comparing the SHG signal of Fig. 6, taken with  $-2$  kV applied across the sample (field parallel to  $-y$  direction), with that of Fig. 7, where an electric field of  $+2$  kV was applied across the sample (field parallel to  $+y$  direction). Typically, application of a step voltage resulted in transient behavior of the second harmonic response, with a fast response on time scales of minutes, followed by a slow response over 1 h, when it reached a steady state. All the measurements of polar plots were performed at this steady state after waiting for a fixed time of 1 h following the application of the field.

As the polar plots become more four lobed, the ratio between the nonlinear coefficients  $K_3$  and  $K_1$  becomes larger. The ratio between these two fit parameters reflects the change in the domain statistics, namely the ratio  $\Delta A_y/\Delta A_x$ . From the fit parameter  $K_2$ , the pure material property, the ratio between  $d_{11}$  and  $d_{12}$  can be calculated. Measurement of the polar plots of the SHG signal were also performed at different values of bias voltages, starting from 0 to  $-2$  kV to  $+2$  kV back to 0 V. From the theoretical fitting of the polar

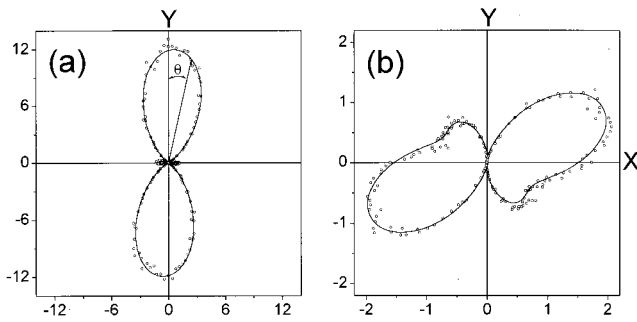


FIG. 7. Polar plots of the SHG intensity  $I^{2\omega}$  ( $\lambda=532$  nm) as a function of input polarization angle  $\theta$  ( $\lambda=1064$  nm) for the output polarization of the SHG light along (a)  $\text{Bi}_4\text{Ti}_3\text{O}_{12}$  [010] (y axis) and (b)  $\text{Bi}_4\text{Ti}_3\text{O}_{12}$  [100] (x axis). The data shown here were measured at room temperature on an as-deposited  $\text{Bi}_4\text{Ti}_3\text{O}_{12}$  film on the  $\text{SrTiO}_3(100)$  substrate with a bias voltage of +2 kV applied across surface electrodes (3 mm apart, see Fig. 4) with the field in the +y direction (see Fig. 1). The experimental data is shown in circles, while the solid line is a nonlinear fit obtained based on Eq. (1) derived from the theoretical model presented in the article. The arrow in (a) represents the magnitude of the SHG light and  $\theta$  indicates the direction of polarization of the fundamental light with respect to the y axis.

plots, one can determine  $I_y^{2\omega}(\theta=0^\circ)$  and  $I_x^{2\omega}(\theta=90^\circ)$ , which in conjunction with a reference measurement from a  $\text{LiTaO}_3$  crystal<sup>7</sup> allows us to calculate the absolute values of  $(\Delta A_y d_{11})^2$  and  $(\Delta A_x d_{11})^2$ , respectively. Figure 8 shows these quantities as a function of applied voltage at room temperature. The arrows in the figure show the time sequence of applied voltages. The thickness fraction values at voltages of +2 and -2 kV were evaluated from polar plots shown in Figs. 6 and 7. While there clearly appear to be changes in domain statistics beyond the error bar, there is no clear trend discernable in these plots, apart from a significant initial increase in  $|\Delta A_x|$  from 0 to -1 kV. This study was the first set of poling experiments performed on the as-deposited thin film. However, as we will show below, this by no means is a unique trend, but rather depends on the history of electric field application. The ratios of nonlinear coefficients were also calculated from the polar plots as a function of applied voltage. The  $d_{11}/d_{12}$  varied from -3.10 to -3.80,  $|d_{26}/d_{11}|$

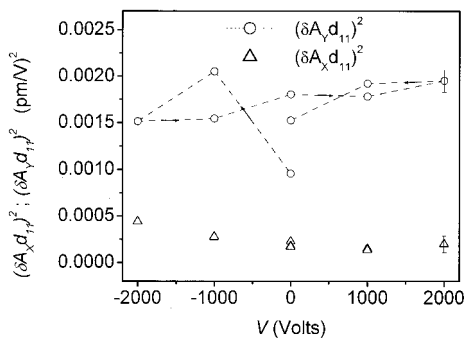


FIG. 8. The variation of the domain bias  $(\Delta A_y)^2$  and  $(\Delta A_x)^2$  at room temperature (23 °C) as a function of the applied voltage across surface electrodes 3 mm apart on a  $\text{Bi}_4\text{Ti}_3\text{O}_{12}$  film on the  $\text{SrTiO}_3(100)$  substrate. The arrows represent the sequence application of the bias voltage across the film. The error bars show the typical magnitude of the measurement error. The domain bias data were extracted from the theoretical analysis of the polar plot measurements such as in Figs. 6 and 7 at different voltage bias values with the field in the  $\pm y$  directions (see Fig. 1).

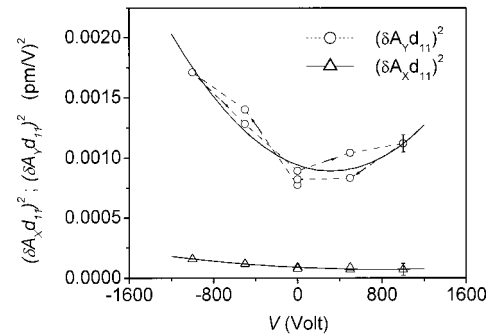


FIG. 9. The net area fraction along the x and y axes  $(\Delta A_y d_{11})^2$  and  $(\Delta A_x d_{11})^2$  at 60 °C as a function of the applied voltage across surface electrodes 3 mm apart on a  $\text{Bi}_4\text{Ti}_3\text{O}_{12}$  film on the  $\text{SrTiO}_3(100)$  substrate. The dashed line connects the experimental data points and the solid line in a polynomial fit as a visual aid. The arrows represent the sequence of application of bias voltage across the film. The error bars show the typical magnitude of the measurement error. The domain bias data were extracted from the theoretical analysis of the polar plot measurements such as in Figs. 6 and 7 at different voltage bias values with fields in the  $\pm y$  directions (see Fig. 1).

varied from 0.31 to 0.43, and the  $|\Delta n|$  varied from 0.035 to 0.149, with no clear trend discernable with voltage for any of these quantities.

A similar experiment was conducted on the same film area at 60 °C with the measurement of polar plots at applied electric fields of up-to  $\pm 1$  kV. Figure 9 shows the changes in domain statistics at 60 °C. The arrows show the time sequence of application of the voltage. The solid line shows a polynomial fit as a visual aid. The results clearly show an increase in  $(\Delta A_y)^2$ , with electric field poling along either polarities in both  $\pm y$  directions, suggesting a domain reorientation process between Y+ and Y- domains. One also notices in Fig. 9 that the  $(\Delta A_x)^2$  changes little over the same electrical field range, suggesting that the movement of nearly -90° domain walls, which couple  $X\pm$  and  $Y\pm$  domain variants, is limited in the domain reorientation process.

Clearly, the Y+(Y-) domains increase in area with electric field along the +y (-y) axis. In this particular instance (Fig. 9), the poling in the -y direction appears stronger than in the +y direction. The minimum in the SHG response therefore appears to be shifted to a slightly positive voltage of  $\sim +250$  V. In the complete phase correlation assumption, the minimum point corresponds to the situation where the net thickness fractions of Y+ and Y- domains are equal in the probe area of the film. This basis indicates that at zero field, the sign of  $\Delta A_y$  is negative, i.e., slightly more Y- domains exist as compared to Y+ domains. Since Eqs. (1) and (6) refer only to even powers of  $\Delta A_y$  (and  $\Delta A_x$ ), one cannot extract the sign of these microstructural quantities from the analysis of polar plots alone. The information on the sign of the bias is new, which can be obtained only by the electric field poling studies just described.

A final aspect to note with respect to  $\Delta A_y$  is that, as defined within the context of complete phase correlation assumption, one would expect that the minimum in SHG intensity in Fig. 9 would go to zero, and therefore  $\Delta A_y=0$  would be expected at this minimum. This is not the case. In

other words, this minimum corresponds to a situation where *equal* thickness fractions of  $Y^+$  and  $Y^-$  domains exist, and the opposite phases of their second harmonic polarization would result in a complete cancellation of the SHG intensity generated from the probe area. This would happen *provided* there is uniform and complete interference of the second harmonic fields generated from all the individual domains, which we refer to as *complete* phase correlation assumption. This assumption, while excellent, clearly is not perfect. A more reasonable assumption is that most of the  $Y^+$  and  $Y^-$  domains are phase correlated, but some are not. The definition of  $\delta A_y$  then needs to be recast as follows:<sup>9</sup>

$$\Delta A_y^2 = \gamma \left[ \int_0^{A_y} (t^{Y^+} - t^{Y^-}) dA^y \right]^2 + (1 - \gamma) \times \left[ \int_0^{A_y} (t^{Y^+} + t^{Y^-}) dA^y \right]^2, \quad (7)$$

where  $0 < \gamma < 1$  represents the *extent of phase correlation*. At the minimum in  $(\Delta A_y d_{11})^2$  in Fig. 9,  $t^{Y^+} \sim t^{Y^-}$ . The second integral inside the square bracket, in Eq. (7) represents the total fraction of  $Y^\pm$  in the film, which can be approximated as  $\sim 0.5$ . Then the value of  $\gamma$  can be estimated from Eq. (7) as  $(1 - \gamma) \sim 4(\Delta A_y d_{11})^2_{\min}$ . This however requires a knowledge of the  $d_{11}$  coefficient in Fig. 9, since experimentally, only the value of  $(\Delta A_y d_{11})^2$  is known.

The material parameters at 60 °C were found to be as follows:  $d_{11}/d_{12}$  varied from  $-2.86$  to  $-3.72$ ,  $|d_{26}/d_{11}|$  varied from 0.29 to 0.46, and the  $\Delta n$  varied from 0.156 to 0.179, with no clear trend discernable with voltage for any of these quantities.

## B. Correlation between electrical conductance and domain state

We present here evidence of a strong correlation between dc conductance and the domain microstructural state in the film at room temperature. Figure 10(a) shows the behavior of the net thickness fraction  $(\Delta A_y d_{11})^2$  along the  $y$  axis, together with the dc electrical current through the sample. This measurement was taken in a *continuous mode*, by fixing the polarizer and the analyzer parallel to the  $y$  axis and measuring the second harmonic response as a function of applied electric fields along  $\pm y$  axes at room temperature. Simultaneous measurement of the current in the external circuit was also performed. Note that the sample probed here (Fig. 10) had a prior history of poling at room temperature (e.g., Fig. 7) and 60 °C (e.g., Fig. 8) before performing this experiment. The first important observation is that the values of currents observed in the poling process are in the 1–10  $\mu$  A range. The total integrated charge under the transient currents due to domain reversal in the film would be expected to be on the order of  $2P_s A \sim 0.3$  nC, where  $P_s \sim 30 \cos 4.5^\circ \mu\text{C}/\text{cm}^2$  is the spontaneous polarization component along the  $a$  axis,<sup>3</sup> and  $A \sim 5 \text{ mm} \times 0.1 \mu\text{m}$  is the cross sectional area of the film under a 5 mm long electrode. However, the experimentally observed electrical currents are up to 9  $\mu\text{A}$ , which translates to 540  $\mu\text{C}/\text{min}$ . Since domain reversal occurs over many minutes, as tracked by the changes in the second har-

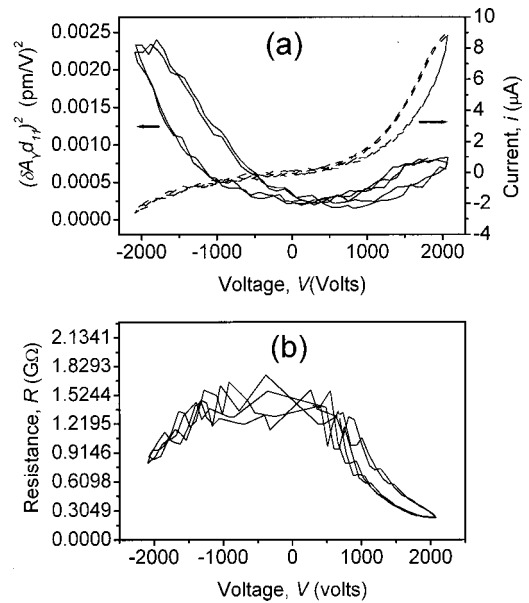


FIG. 10. (a) The net area fraction along the  $y$  axis  $(\delta A_y d_{11})^2$  and the dielectric loss currents  $i$  through the sample at room temperature (23 °C), while continuously varying the bias voltage  $V$  (field along  $\pm y$  directions; see Fig. 1) across surface electrodes, 3 mm apart (see Fig. 4) on a  $\text{Bi}_4\text{Ti}_3\text{O}_{12}$  film on the  $\text{SrTiO}_3(100)$  substrate. (b) The resistance of the film  $R = V/i$  as a function of the applied voltage  $V$  showing asymmetry between the positive and negative voltages.

monic output, clearly the total integrated charge under the observed currents is much larger than that expected under transient currents due to domain reversal. Further the observed currents reach a steady state and remain as long as the applied voltage is on, unlike transient currents, which occur only during domain reversal. We therefore conclude that the currents in Fig. 10 primarily arise from the dielectric losses in the film.

Despite this, one finds a clear inverse correlation between the observed electrical currents in the film and the intensity of the SHG signal, namely, that *smaller second harmonic signal results in larger electrical currents, and vice versa*. This phenomenon was observed consistently at room temperature and at 60 °C under various sample poling histories and applied voltages. Since the second harmonic generation signal is directly related to the domain state, namely,  $I_y^{2\omega} \propto (\Delta A_y)^2$ , the larger the relative domain bias  $\Delta A_y$ , the smaller the leakage current through the film, and vice versa. This correlation is better understood in terms of the resistance  $R$  in the film, given by  $R = V/i$ , where  $V$  is the applied voltage and  $i$  the electrical current. Figure 10(b) plots the electrical resistance  $R$  as a function of the applied voltage  $V$ . The resistance  $R$  decreases with increasing voltage in a non-linear way. However, the decrease is *not* symmetric with respect to the polarity of the applied voltage; the resistance is  $\sim 4$  times *larger* at +2 kV as compared to  $-2$  kV. On the other hand, from Fig. 10(a), the domain bias  $(\Delta A_y d_{11})^2$  at +2 kV is  $\sim 3$  times *smaller* than the value of  $-2$  kV, thus clearly demonstrating the inverse correlation between domain bias and electrical resistance.

We propose that the physical bias for this inverse correlation between  $(\Delta A_y)^2$  and  $R$  arises from the creation and

destruction of charged domain walls within the film. When the domain bias  $\Delta A_y$  is small, the relative population of the  $Y+$  and the  $Y-$  domains are approximately equal. In this state, there is a high density of *charged* domain walls, arising from domains of type II (see Fig. 2), with walls of (100)  $b-c$  crystallographic planes perpendicular to the growth plane, and those of type III, with walls of (001)  $a-b$  crystallographic planes parallel to the growth plane. Upon application of an electric field along the  $\pm y$  direction, the population of  $Y+$  or  $Y-$  increases with respect to the other variant, and consequently, the magnitude of  $\Delta A_y$  increases and the density of charged domain walls decreases. Charged domain walls, both parallel (such as walls III) and transverse (such as walls II) to the direction of net current flow, enhance the electrical conduction by providing alternate “easy” conduction paths. More precisely, upon application of a voltage and flow of some initial leakage current, a newly created *charged* domain wall will, in the initial period act as a sink of charges. However, the amount of charge required to achieve this in this film is at most on the order of nanoCoulombs, as we estimated earlier. Therefore, the charged walls are neutralized rather easily. Once a charge compensated domain wall plane is present, it no longer acts as a sink, but rather as a charge plane, which facilitates further electrical conduction by allowing a steady state flow of compensating charge through this plane for a given applied voltage. Even charged domain walls transverse to the net flow of current can help by removing bottlenecks in the flow of current and providing alternate paths for conduction through lateral movement of charge at the sites of bottlenecks.

The above discussion would lead to the qualitative conclusion that the *decrease* in the density of charged domain walls in the film through electric field poling results from an *increase* in the domain bias  $\Delta A_j$  (for field along the direction  $j$ ), and a simultaneous decrease in the number of electrical conduction paths, and therefore an *increase* in the resistance of the film for a given applied voltage. These are precisely the correlations deduced from Fig. 10.

It should be noted that such experimental correlations are possible in this case only because we can determine the

ferroelectric domain state of the film (by second harmonic generation) independent of the electrical current measurements.

## V. CONCLUSIONS

This work has presented electric field induced domain rearrangement studies in bismuth–titanate thin films using *in situ* second harmonic generation. The theoretical treatment of the spatial symmetries of second harmonic generation signal from the film yields quantitative information on basic material properties, such as the determination of the ratios of nonlinear coefficients,  $d_{12}/d_{11}$ ,  $|d_{26}/d_{12}|$ , and  $|d_{26}/d_{11}|$ . In addition, the thickness fractions  $\Delta A_x$  and  $\Delta A_y$ , representing the ratio of the *net* fraction of the  $a$  component of polarization in the  $x$  or the  $y$  directions, could be determined sensitively in the probed area (see text for definitions). These parameters are tracked in real time as a function of applied voltage, and the ferroelectric polarization hysteresis curves deduced from the measurements. We also found a strong correlation between the dc electrical leakage current through the film and the ferroelectric domain state of the film, as deduced from the second harmonic measurements. A qualitative model for this correlation is based on the creation and destruction of charged domain walls in the film.

## ACKNOWLEDGMENTS

We gratefully acknowledge the financial support of the National Science Foundation through Grants DMR-9984691 and DMR-0103354.

<sup>1</sup>C. A. Paz de araujo, J. D. Cuchiaro, L. D. McMillan, M. C. Scott, and J. F. Scott, *Nature (London)* **374**, 627 (1995).

<sup>2</sup>R. E. Newnham, R. W. Wolfe, and J. F. Dorrian, *Mater. Res. Bull.* **6**, 1029 (1971).

<sup>3</sup>S. E. Cummins and L. E. Cross, *J. Appl. Phys.* **39**, 2268 (1968).

<sup>4</sup>Y. Barad, J. Lettieri, C. D. Theis, D. G. Schlom, V. Gopalan, J. C. Jiang, and X. Q. Pan, *J. Appl. Phys.* **89**, 1387 (2001); **89**, 5230 (2001).

<sup>5</sup>C. D. Theis, J. Yeh, D. G. Schlom, M. E. Hawley, G. W. Brown, J. C. Jiang, and X. Q. Pan, *Appl. Phys. Lett.* **72**, 2817 (1998).

<sup>6</sup>A. D. Rae, *Acta Crystallogr., Sect. B: Struct. Sci.* **B46**, 474 (1990).

<sup>7</sup>V. Gopalan and R. Raj, *J. Am. Ceram. Soc.* **79**, 3289 (1996).

<sup>8</sup>W. L. Bond, *J. Appl. Phys.* **36**, 1674 (1965).

<sup>9</sup>V. Gopalan and R. Raj, *J. Appl. Phys.* **81**, 865 (1997).